ACS APPLIED MATERIALS & INTERFACES

Research Article

www.acsami.org

Improving Performance and Lifetime of Small-Molecule Organic Photovoltaic Devices by Using Bathocuproine–Fullerene Cathodic Layer

Shun-Wei Liu,*[,†,§] Chih-Chien Lee,*[,‡,§] Wei-Cheng Su,[‡] Chih-Hsien Yuan,[‡] Yi-Sheng Shu,[†] Wen-Chang Chang,[‡] Jhih-Yan Guo,[†] Chien-Feng Chiu,[†] Ya-Ze Li,[†] Tsung-Hao Su,[†] Kuan-Ting Chen,[‡] Po-Chien Chang,[†] Tzu-Hung Yeh,[†] and Yu-Hsuan Liu[‡]

[†]Department of Electronic Engineering, Ming Chi University of Technology, No. 84, Gungjuan Road, Taishan District, New Taipei City 24301, Taiwan

[‡]Department of Electronic Engineering, National Taiwan University of Science and Technology, No. 43, Section 4, Keelung Road, Daan District, Taipei 10607, Taiwan

Supporting Information

ABSTRACT: In this study, we compared the use of neat bathocuproine (BCP) and BCP:C_{60} mixed buffer layers in chloroboron subphthalocyanine (SubPc)/C_{60} bilayer organic photovoltaic (OPV) devices and analyzed their influence on device performance. Replacing the conventional BCP with BCP:C_{60} enabled manipulating the optical field distribution for optimizing the optical properties of the devices. Estimation of the interfacial barrier indicated that the insertion of the BCP:C_{60} between the C_{60} and electrode can effectively reduce the barrier for electrons and enhance electron collection at the electrode. Temperature-dependent measurements of the OPV devices performed to calculate the barrier height at the SubPc/C_{60} interface suggested that band bending was larger when the BCP:C_{60} buffer layer was used, reflecting increased exciton dissociation efficiency. In addition, the device lifetime was considerably improved when the BCP:C_{60} buffer layer was used. The device performance was stabilized after the photodegradation of the active layers, thereby increasing the device lifetime compared with the use of the neat BCP buffer layer. Atomic force microscopy images showed that the neat BCP was easily crystallized and could degrade the cathodic interface, whereas the blend of C_{60} and BCP suppressed the crystallization of BCP. Therefore, the optimal buffer layer improved both the device performance and the device lifetime.

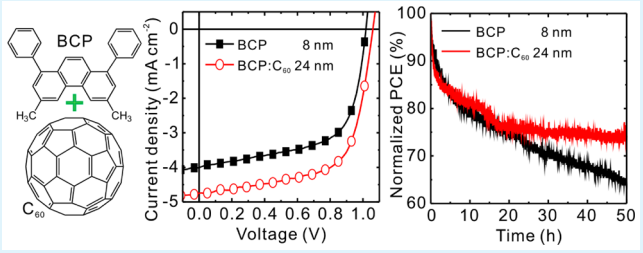

KEYWORDS: *small-molecule organic photovoltaic, power conversion efficiency, lifetime, cathodic buffer layer, optical manipulation, morphology*

INTRODUCTION

Small-molecule organic photovoltaic (OPV) devices have the potential to be next-generation photovoltaic devices because their power conversion efficiency (PCE) has substantially improved over the past decade.[1−3] One of the major developments is the evolution of cathodic buffer layers.[4−10] Unlike inorganic semiconductors, in these layers strong binding between electrons and holes leads to the formation of excitons (i.e., strongly bound electron−hole pairs).[11] These excitons must diffuse to the donor/acceptor interface to overcome the binding energy and dissociate into free electrons and holes.[12] Conventional OPV devices use fullerenes such as C_{60} and C_{70} as an acceptor; fullerenes have a large excition diffusion length.[13−15] Therefore, an exciton-blocking layer (EBL) is necessary to prevent the quench of excitons near the electrode and thereby increase the possibility of exciton dissociation.[16−18] In our previous studies, we demonstrated that the thickness variation of C_{60} and C_{70} enables manipulating the optical field distribution in OPV devices with different donor materials.[19,20] This optical tuning property is a consequence of the first optical field maximum occurring close to the reflective metal because of optical interference.[21−23] However, the wide absorption band of C_{60} and C_{70} may increase unnecessary absorption in OPV devices.[24,25] Therefore, using C_{60} and C_{70} as optical spacers may be inappropriate for optical field manipulation.

In contrast to fullerene, a wide band gap EBL that is transparent to visible light is a promising candidate for an optical spacer.[26−29] For example, the conventional EBLs, bathacoproine (BCP) and bathophenanthroline (BPhen), are typically used to block excitons and act as electron selective layers.[4,7,13,30−33] However, the ability to transport electrons is attributed to carrier hopping through defect sites formed during

Received: March 3, 2015
Accepted: April 14, 2015
Published: April 14, 2015

DOI: 10.1021/acsami.5b01888
ACS Appl. Mater. Interfaces 2015, 7, 9262−9273

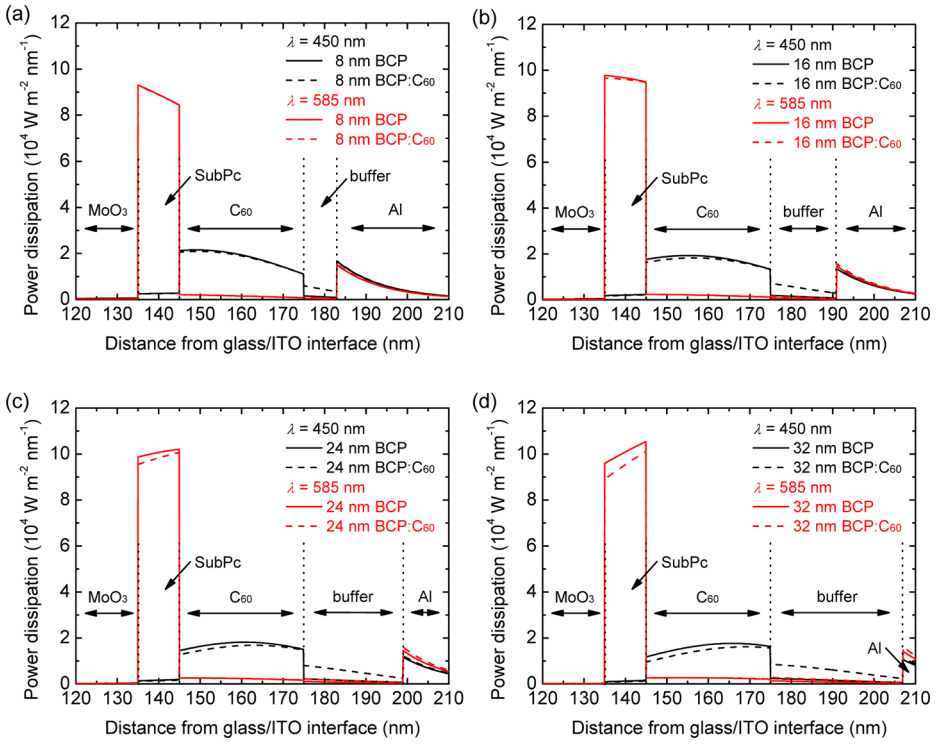

Figure 1. Power dissipation profiles of OPV devices with neat BCP and BCP:C_{60} mixed buffer layers of various thicknesses, (a) 8, (b), 16, (c) 24, and (d) 32 nm, at incident wavelengths of 450 and 585 nm, which correspond to the peak absorption of C_{60} and SubPc, respectively (Supporting Information Figure S1). The solid and dashed lines denote devices with BCP and BCP:C_{60} buffer layers, respectively.

the deposition of metal cathodes.[13,30,34,35] Because of the limited penetration depth of the metal atoms, the number of defect sites of BCP and BPhen may be reduced as a function of the BCP and BPhen thicknesses, thus restricting the thickness to typically less than 10 nm, as shown by previous studies.[5,7,8,10,13,31,32] Nevertheless, using the conventional EBLs is advantageous because the embedded optical spacer can be used, implying that additional layers need not to be introduced; introducing additional layers complicates the fabrication processes of the OPV devices. Metal-doped EBLs have been proposed for facilitating efficient electron conduction and blocking excitons simultaneously.[6,32] Multilayer structures have been used as EBLs and optical spacers.[8−10,33] Although the device performance considerably improves when multilayer EBLs are used, the insertion of additional layers is unfavorable for simplifying the device structure.

Recently, Luo et al. employed LiF as a dopant for the C_{60} layer, and a thin layer of BCP (i.e., C_{60}:LiF/BCP) was deposited over the C_{60} layer to optimize the optical properties and exciton energy transfer.[36] Menke et al. proposed using a dilute acceptor layer prepared from a blend of C_{60} and a wide band gap material, *p*-bis(triphenylsilyl)benzene (UGH2), to enhance light absorption.[37] By appropriately controlling the concentration of UGH2 and the thickness of the dilute layer, more efficient use of absorbed photons at the donor/acceptor interface was achieved, leading to a large enhancement of the short-circuit current density (J_{SC}) compared with the neat C_{60} layer. This concept is similar to that presented by Luo et al., who suggested doping the C_{60} with wide band gap, transparent materials. Bartynski et al. reported a simplified EBL prepared from a blend of C_{60} and BCP that showed high electron conductivity and efficient exciton blocking effects.[38] A crucial finding relating to the BCP:C_{60} buffer layer was the low exciton−polaron recombination at the acceptor/EBL interface, which may reduce exciton dissociation and hence J_{SC}. Xiao et al. used the same concept but a different material, BPhen:C_{60}, to increase exciton dissociation and electron extraction, thereby improving the fill factor (FF).[39]

In the current study, we demonstrated the high PCE and long device lifetime of chloroboron subphthalocyanine (SubPc)/C_{60}-based small-molecule OPV devices containing a mixed EBL comprising BCP and C_{60}. Although the concept is not new, we thoroughly studied the capability to tune the optical field distribution, properties of the C_{60}/buffer layer interface, morphological changes, and diode behavior associated with the use of the BCP:C_{60} buffer layer. An optical simulation was performed to calculate the power dissipation profile inside the OPV devices. Optimal optical properties can be achieved by using a 24 nm buffer layer. However, the conventional BCP layer has a thickness of less than 10 nm, preventing optical field manipulation. By contrast, the BCP:C_{60} buffer layer shows satisfactory electrical conduction for a thickness of 24 nm, thereby showing the ability to tune the optical properties of the OPV devices. A series of temperature-dependent measurements was performed to estimate the effective interfacial barrier at the C_{60}/buffer layer interface and the barrier height at the SubPc/C_{60} interface. The results suggested that using an optimal BCP:C_{60} buffer layer improves both the charge collection efficiency and exciton dissociation, thereby enhancing the PCE considerably. In addition, because the BCP crystallization is suppressed by C_{60}, the device with the BCP:C_{60} buffer layer shows a much longer lifetime and almost stable performance over time compared with a device using neat BCP.

DOI: 10.1021/acsami.5b01888
ACS Appl. Mater. Interfaces 2015, 7, 9262−9273

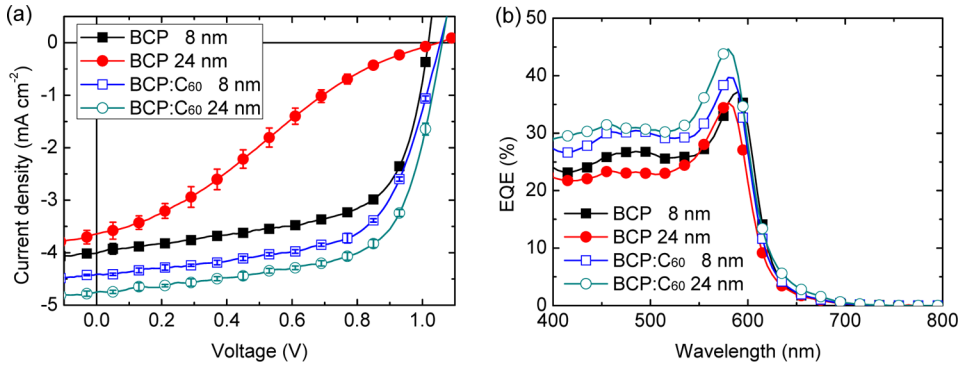

Figure 2. (a) Photo $J-V$ characteristics of OPV devices with various buffer layers under AM 1.5G solar illumination at 100 mW cm^{-2}. The error bars shown were determined by examining 10 devices. (b) EQE spectra of OPV devices with various buffer layers. The solid and open symbols denote devices with BCP and BCP:C_{60} buffer layers, respectively.

Table 1. Photovoltaic Parameters of OPV Devices with Various Buffer Layers under AM 1.5G Solar Illumination at 100 mW cm^{-2}[a]

device	V_{OC} (V)	J_{SC} (mA cm^{-2})	FF (%)	PCE (%)
BCP, 8 nm	1.02 ± 0.004	4.0 ± 0.01	62 ± 0.1	2.5 ± 0.03
BCP, 24 nm	1.05 ± 0.007	3.6 ± 0.13	26 ± 2.0	1.0 ± 0.09
BCP:C_{60}, 8 nm	1.06 ± 0.004	4.4 ± 0.05	63 ± 0.5	2.9 ± 0.02
BCP:C_{60}, 24 nm	1.06 ± 0.005	4.7 ± 0.05	64 ± 0.9	3.2 ± 0.06

[a]The standard deviations for an average of 10 devices are provided.

RESULTS AND DISCUSSION

To demonstrate the optical field tunability of the device with the BCP:C_{60} buffer layer, power dissipation profiles were calculated using the transfer matrix method[40] for OPV devices with the structure indium tin oxide (ITO)/MoO_3 (15 nm)/SubPc (10 nm)/C_{60} (30 nm)/BCP or BCP:C_{60}/Al (120 nm). In the current study, the mixing ratio of BCP:C_{60} was 1:1 (volume ratio). The chosen mixing ratio was referenced to previous study, which has presented the optimal device performance through the use of a 1:1 mixing ratio of BCP (or BPhen) to C_{60} as a buffer layer.[38] The optical constants used in the calculation are provided in the Supporting Information (Figure S1). The calculated power dissipation profiles provided direct evidence of photon absorption by the active layers.[20] Figure 1 shows the calculated results. All devices showed similar profiles, and there were slight differences between the profiles of the device with a BCP buffer layer and that of the device with a BCP:C_{60} buffer layer. Because the photocurrent in SubPc is likely to be higher than that in C_{60} because of the considerably high absorption of SubPc, the following discussion focuses on the SubPc layer. The power dissipation of the device with the BCP:C_{60} mixed buffer layer was slightly lower than that that of the device with neat BCP. A possible reason for the difference is the expense of the photon absorption in the BCP:C_{60} buffer layer. The device with an 8 nm buffer layer exhibited an undesirable profile because the maximal photon absorption occurred at the MoO_3/SubPc interface instead of the SubPc/C_{60} interface, where exciton dissociation occurs (Figure 1a). A similar profile was observed for the device with a 16 nm buffer layer despite a higher absorption intensity (Figure 1b). When the thickness of the buffer layer was increased to 24 nm, the maximum power dissipation was appropriately located at the SubPc/C_{60} interface (Figure 1c). However, a 32 nm device exhibited a decreased tail in the profile, which may reduce the photocurrent because of low photon absorption (Figure 1d). These results suggest that the optical field distribution of OPV devices can be optimized by using a buffer layer with a thickness of 24 nm.

Figure 2a shows the photo $J-V$ characteristics of the OPV devices with various buffer layers under AM 1.5G solar illumination at 100 mW cm^{-2}. All of the data were obtained from 10 devices on two different substrates, and the error bars for each cell parameter are provided in the figure. The device with a standard configuration (i.e., with an 8 nm thick BCP layer) showed a conventional curve, similar to that observed in previous studies where SubPc was used as the donor.[41,42] However, when the thickness of the BCP was increased to 24 nm, the rectification characteristics of the diode deteriorated and conformed to an s-shaped-like curve. The s-shaped curve can be attributed to charge accumulation, the presence of an interface dipole, an energy difference between two sides of the organic/metal interface, chemical degradation at the electrode interface, and an imbalance between the hole and the electron mobility.[43−48] In the current study, the s-shaped curve was attributed to poor electron extraction because of the low number of defect states near the C_{60}/BCP interface. Under a small forward bias, the built-in potential is compensated for by the external applied bias, thus resulting in charge accumulation at the C_{60}/BCP interface.[48] Although J_{SC} remained similar to that of an 8 nm BCP, the s-shaped curve reduced the FF and hence the PCE, as shown in Table 1. These results suggest that achieving the optical tuning by varying the thickness of the neat BCP buffer layer is impossible. By contrast, the devices with the 8 and 24 nm BCP:C_{60} buffer layers showed standard rectification characteristics and, thus, identical FFs. Nevertheless, because the optical properties in the OPV devices were shown to be optimal for the thickness of 24 nm, as shown in Figure 1, J_{SC} was slightly higher in the device with the 24 nm BCP:C_{60} buffer layer. The PCE of the devices with various BCP:C_{60} thicknesses was therefore optimized from 2.9% to 3.2% (Supporting Information Figure S2). We have previously reported a series of high efficiency SubPc/C_{60} devices through

DOI: 10.1021/acsami.5b01888
ACS Appl. Mater. Interfaces 2015, 7, 9262−9273

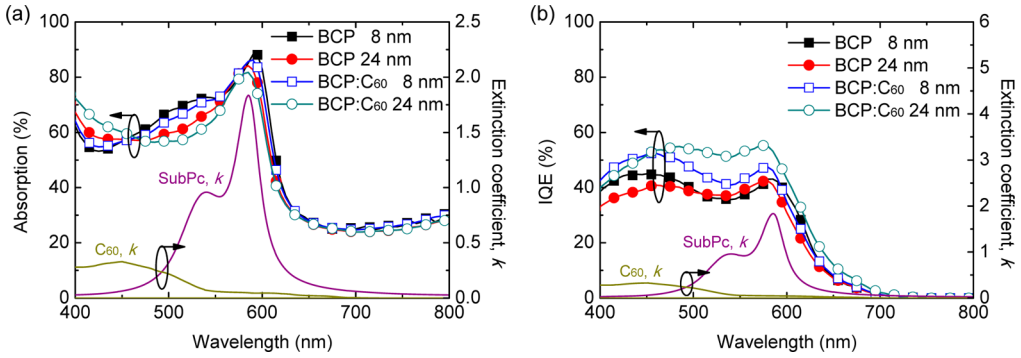

Figure 3. (a) Total absorption and (b) IQEs of OPV devices with various buffer layers. The solid and open symbols denote devices with BCP and BCP:C_{60} buffer layers, respectively. Extinction coefficients of neat SubPc and C_{60} layers are indicated by solid lines.

the control of fabrication process and materials preparation, which yielded the PCE approaching 4.0%.[49−52] However, in the current study, the standard device showed a PCE of 2.5% only. The reason for the lower PCE here is that SubPc was used as received without further purification. In addition, all devices with various buffer layers were simultaneously fabricated through a homemade independently controlled shutter system, which allows for producing at most four different cell parameters. Therefore, the improvement in device performance primarily resulted from the use of the different buffer layers without run-to-run deviation. In addition to the improvement in the PCE, all of the devices with a BCP:C_{60} buffer layer showed similar performance. Their similar performance indicates the extent of the thickness tuning window. Figure 2b shows the external quantum efficiency (EQE) spectra of the OPV devices with various buffer layers. Because J_{SC} is linearly proportional to the product of the EQE and the AM 1.5G solar spectrum, the EQE values were directly reflected by the trend of the experimental J_{SC}. The shape of EQE spectra varied with the buffer layer used. This result is primarily caused by optical field manipulation. In addition, for the thickness of 24 nm, irrespective of the type of buffer layer used, the peak wavelength of the EQE shifted toward the absorption maximum of SubPc. This observation indicates that the optical field distribution in the 24 nm devices was optimized, regardless of whether BCP or BCP:C_{60} was used as the buffer layer, as predicted in Figure 1. Although the optical field manipulation can contribute to the increase in J_{SC}, there are possible mechanisms in increasing J_{SC} such as internal quantum efficiency and carrier collection efficiency, both of which will be discussed later. To resolve the contribution of the optical field manipulation, a model to predict the trend in the J_{SC} change is much appropriate. However, in the current study, we cannot predict the J_{SC} change because of two reasons. First, the transportation of electrons is generally via the defect sites caused through the deposition of electrode; the penetration depth of metal atoms to create defect sites is limited and renders the model complex. In previous study, Wang and co-workers have predicted the s-shape trend with various thicknesses of BCP.[48] However, the predicted J_{SC} remained the same. Second, the electron transport via the BCP:C_{60} buffer layer is still unclear, probably because of defect sites in BCP and/or direct transport in C_{60}. To predict J_{SC} and quantify the contribution of optical field manipulation, detailed physical mechanisms should be accounted for.

Neat BCP is transparent to the wavelength range of the SubPc absorption band (Supporting Information Figure S1). When BCP was doped with C_{60} to form the mixed buffer layer, the transparency of the buffer layer changed because of the absorption of the C_{60}. The variation in the transparency resulting from the use of different buffer layers led to a change in the absorption spectra of the OPV devices. To investigate the absorption change, total absorption measurement was conducted using an integrating sphere in the reflection mode (Supporting Information Figure S3). The integrating sphere accounts for optical interference, scattering from each interface, and electrode absorption and precisely estimates the reflection of OPV devices.[53] By subtracting unity from the reflection, the total absorption of the OPV devices can be obtained. Figure 3a shows the total absorption of the OPV devices with various buffer layers. For comparison, the extinction coefficients of neat SubPc and C_{60} are provided. The absorption peaks of the devices showed a slight shift from approximately 590−595 to 585 nm, irrespective of the type of the buffer layer, when the thicknesses of the buffer layers were increased from 8 to 24 nm. This result indicates that the thickness of 24 nm enables manipulation of the optical properties, as predicted in Figure 1. Because of the presence of C_{60}, the devices with a BCP:C_{60} buffer layer showed a slight decrease in absorption in a wavelength range of 450−600 nm compared with the devices with neat BCP as the buffer layer. Although the recoupling effect from the buffer layer containing C_{60} increased the absorption in a wavelength range of 400−450 nm, the J_{SC} may not be improved because the solar spectrum exhibits a lower intensity in this wavelength range. In addition to the optical manipulation, an increase in charge collection may contribute to an increase in J_{SC}. To determine whether using a BCP:C_{60} buffer layer can increase the charge collection efficiency, the internal quantum efficiency (IQE) was determined by dividing the EQE by the absorption. As shown in Figure 2b, for the thickness of 8 nm, the IQE of the device with the BCP:C_{60} buffer layer increased over the entire spectrum. In addition, when the thickness of the BCP:C_{60} buffer layer was increased to 24 nm, the IQE was highly superior to the IQEs of other devices with different buffer layers, especially in the wavelength range of approximately 500−600 nm. These results indicate that the charge collection efficiency can be considerably improved by either using the mixed buffer layer or optimizing the thickness. Therefore, using the optimal buffer layer improves not only the optical properties but also the charge collection efficiency and hence J_{SC}. With an improved IQE, typically an improved FF may be expected. However, in the studied devices there is a slight dependence of FF under the influence of buffer layers. In bilayer OPV devices, the FF can

DOI: 10.1021/acsami.5b01888
ACS Appl. Mater. Interfaces 2015, 7, 9262−9273

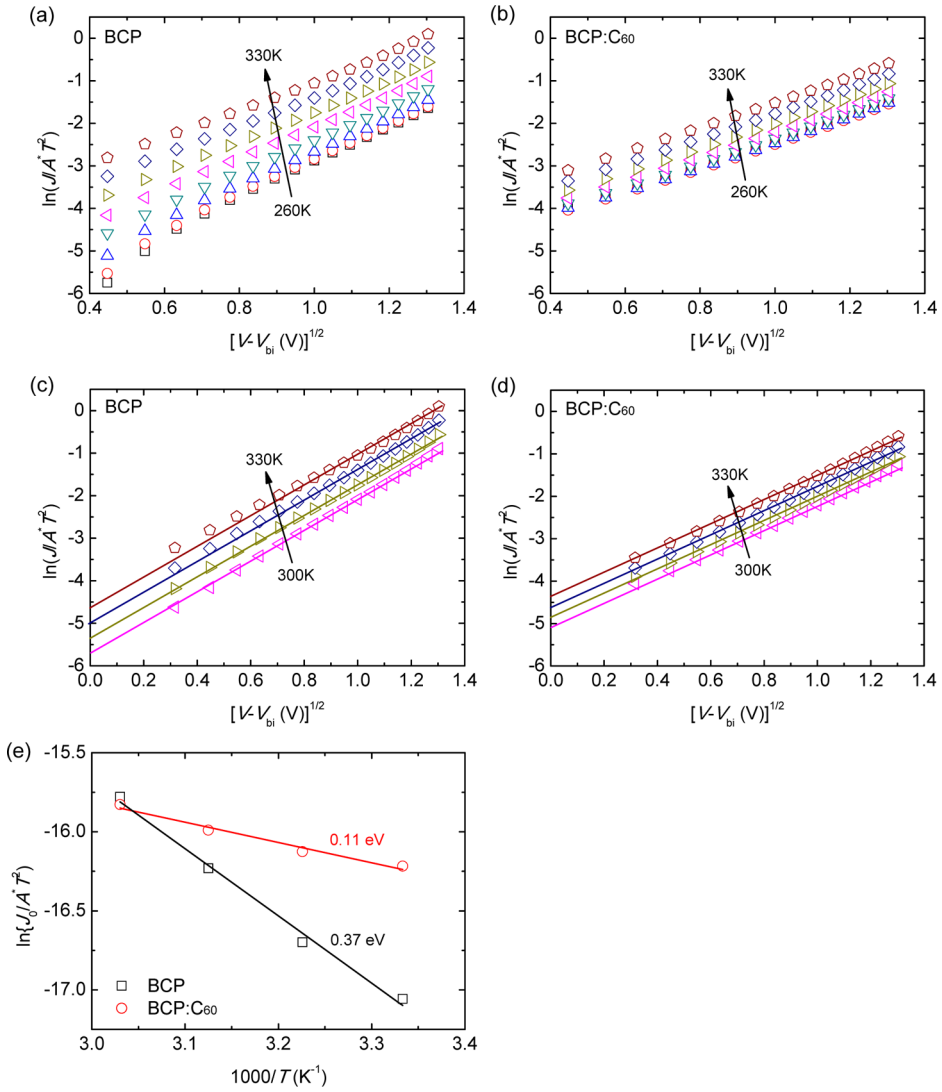

Figure 4. Plot of $\ln(J/A^*T^2)$ versus $(V - V_{bi})^{1/2}$ for the electron-only devices with (a) BCP and (b) BCP:C_{60} buffer layers in a temperature range of 260−330 K. Plot of $\ln(J/A^*T^2)$ versus $(V - V_{bi})^{1/2}$ for the electron-only devices with (c) BCP and (d) BCP:C_{60} buffer layers in a temperature range of 300−330 K for estimating the field-free current density J_0. The intercept enables calculating J_0 by taking the exponent of the intercept. (e) Plot of $\ln(J_0/A^*T^2)$ as a function of $(1000/T)$ for estimating the effective interfacial barrier Δ_B.

reach its highest value if the device structure was optimized.[20,54] In the current study, the device structure was almost optimized through the control of the SubPc and C_{60} thicknesses. Therefore, the improved IQE primarily contributed to the increase in J_{SC} while maintaining the high FF.

To determine the improvement in the charge collection efficiency, temperature-dependent measurement of electron-only devices was conducted to estimate the interfacial barrier at the C_{60}/buffer layer interface. The electron-only devices had the structure Al (100 nm)/BCP or BCP:C_{60} (8 nm)/C_{60} (150 nm)/LiF (1 nm)/Al (100 nm). LiF/Al has been shown to provide an effective quasiohmic contact with C_{60}.[55] When a positive bias and a negative bias are applied to Al near the buffer layer and Al near LiF electrodes, respectively, holes are blocked at the Al/BCP interface because of the large interfacial barrier; however, electrons can enter the device across the quasiohmic contact. Because of the high electron mobility of C_{60}, electrons were rapidly transported through the C_{60} layer and encountered a barrier at the C_{60}/BCP interface before their collection at the Al electrode. The interfacial barrier was estimated on the basis of the framework of the Schottky emission current density, and it can be expressed as follows:[56]

$$J = A^*T^2 \exp\langle -q\{\Delta_B - [q(V - V_{bi})/4\pi\varepsilon_r\varepsilon_0 kd]^{1/2}\}/kT\rangle \quad (1)$$

Here, A^* is the effective Richardson constant, which depends on the effective mass; T is the temperature; q is the elementary charge; Δ_B is the interfacial barrier; V is the applied voltage; V_{bi} is the built-in potential; ε_r and ε_0 are the relative dielectric constant and permittivity of free space, respectively; k is the Boltzmann constant; and d is the thickness of the C_{60} layer. In the plot of $\ln(J/A^*T^2)$ versus $(V - V_{bi})^{1/2}$, a linear relation indicates that the current injection is dominated by the Schottky energy barrier. In the current study, a wide temperature range of 260−330 K was considered to ensure the applicability of eq 1. The parameter V_{bi} of the electron devices was assumed to be zero because the same Al electrode was used. Parts a and b of Figure 4 show the experimental results for the electron-only devices with BCP and BCP:C_{60} buffer layers, respectively. At low temperatures, electrons

DOI: 10.1021/acsami.5b01888
ACS Appl. Mater. Interfaces 2015, 7, 9262−9273

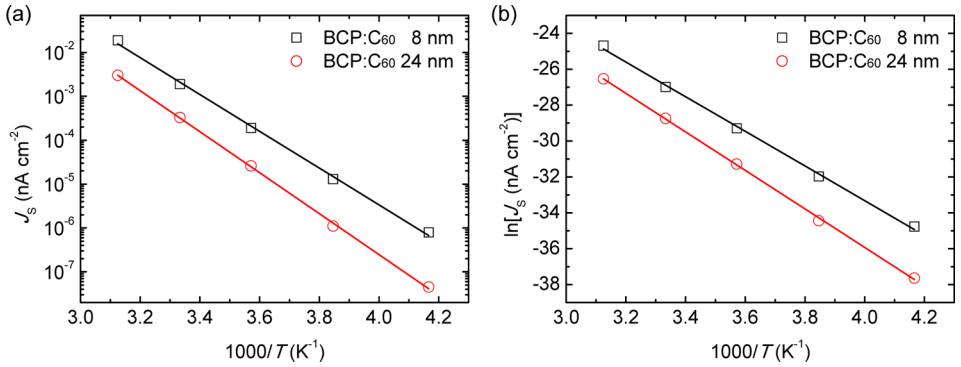

Figure 5. (a) Variation of the calculated J_0 as a function of $(1000/T)$ for the OPV devices with different BCP:C_{60} thicknesses. (b) Plot of $\ln(J_S)$ versus $(1000/T)$, used for estimating Φ_B at the SubPc/C_{60} interface. The open symbols and solid lines represent fits for eqs 3 and 4, respectively.

cannot cross the C_{60}/BCP and C_{60}/BCP:C_{60} interfaces, and therefore, the device with both types of buffer layers exhibited similar low currents (Supporting Information Figure S4a,b). The currents increased appreciably in the temperature range of 280−290 K in both the BCP and BCP:C_{60} devices. However, the increase in the BCP device was larger, indicating the presence of a larger interfacial barrier in this device. Although the electron transport in the buffer layers generally occurs through carrier hopping between defects, the linear relation in the $\ln(J/A^*T^2)$ versus $(V - V_{bi})^{1/2}$ plots strongly suggests the dominance of Schottky emission. Therefore, the current densities in both devices are analogous to the Schottky emission current density, thus implying the applicability of eq 1 to the electron-only devices. The interfacial barrier can be estimated from the field-free current density, J_0, which can be obtained from the following expression:

$$J_0 = A^*T^2 \exp(-q\Delta_B/kT) \tag{2}$$

J_0 was obtained by extrapolating a straight line that fits the linear region to the zero field (i.e., $(V - V_{bi})^{1/2} = 0$) and calculating the exponent of the intercept, as shown in Figure 4c,d. The term $\ln(J_0/A^*T^2)$ can be plotted as a function of $(1000/T)$, and Δ_B can be obtained from the slope of the curve. Despite the dominance of Schottky emission, the fits of estimates of Δ_B did not agree with the predictions in the low temperature range (Supporting Information Figure S4c). A possible reason for this disagreement is the perturbation of defect-induced electron transport. Nevertheless, the fitting results presented an approximation for estimating the effective Δ_B, as shown in Figure 4e. For the devices with BCP and BCP:C_{60} buffer layers, the Δ_B values were approximately 0.37 and 0.11 eV, respectively. A decrease in Δ_B enables electrons to cross the C_{60}/buffer layer interface more efficiently, leading to higher charge collection efficiency, as observed in the IQE spectra.

The use of C_{60} to form the mixed buffer layer has been shown to be effective in reducing the interfacial barrier, thereby increasing the electron collection efficiency at the electrode. As shown in Figure 3b, the IQE of the device with a 24 nm BCP:C_{60} buffer layer was considerably higher compared with that of the device with an 8 nm BCP:C_{60} buffer layer. To determine the extent of improvement, the barrier height at the SubPc/C_{60} interface was investigated in the OPV devices by using the BCP:C_{60} buffer layer with different thicknesses. The $J-V$ characteristics of OPV devices can be described by the following generalized diode equation:[57]

$$J = \frac{1}{1 + R_S/R_{SH}}\left\{J_S\left[\exp\left(\frac{V - JR_SA}{nkT/q}\right) - 1\right] - \left(J_{PH} - \frac{V}{R_{SH}A}\right)\right\} \tag{3}$$

In eq 3, R_S and R_{SH} are the series and shunt resistances (in ohms), J_S is the reverse dark saturation current density, A is the active area of the device, n is the diode ideality factor, and J_{PH} is the photocurrent. Because of the trap-rich nature of organic materials, the fits of the experimental dark $J-V$ curves to eq 3 usually yield inconsistent results in the range of either high reverse or small forward biases.[17,57−59] Therefore, we propose a modified model by replacing R_{SH} with a bias-dependent term, $R_{SH0} \pm \beta V R_{SH0}$, where β represents the trap dependence and the operation (addition or subtraction) depends on the polarity of the applied bias.[20] The proposed modified model can precisely predict the $J-V$ curves under reverse biases (Supporting Information Figure S5). Although the modified model cannot fit the experimental results for small forward biases, as shown in the insets of Supporting Information Figure S5, the fits were consistent with the $J-V$ curves for higher biases. The parameter J_S in eq 3 can be expressed by the thermally activated injection expression:[58]

$$J_S = J_{S0} \exp(-\Phi_B/kT) \tag{4}$$

Here, J_{S0} is a prefactor depending on material properties and Φ_B is the barrier height. The barrier height can be determined from the slope in the plot of $\ln(J_S)$ versus $(1000/T)$. Figure 5a shows the calculated J_S as a function of the temperature. Figure 5b shows the fitting results for eq 4. The values of Φ_B estimated from Figure 5b are 0.83 and 0.93 eV for the OPV devices with 8 and 24 nm BCP:C_{60} buffer layers, respectively. The device with a 24 nm BCP:C_{60} buffer layer showed a higher Φ_B, indicating larger band bending at the SubPc/C_{60} interface. The larger band bending is associated with more efficient exciton dissociation at the SubPc/C_{60} interface. In addition, in Figure 3b, the devices with a 24 nm BCP:C_{60} buffer layer showed the improvement in IQE over the spectrum which SubPc absorbs. This may indicate the energetic change in the device; the LUMO−LUMO (LUMO = lowest unoccupied molecular orbital) offset between SubPc and C_{60} in the device with a 24 nm BCP:C_{60} buffer layer was larger than the device with an 8 nm BCP:C_{60} buffer layer. Therefore, excitons in SubPc can overcome the exciton binding energy more easily and allows for more carrier generation and, hence, the J_{SC}. This phenomenon is probably due to the reduction in electron accumulation in C_{60} because of the reduced exciton−polaron quenching at the C_{60}/BCP:C_{60} interface.[38] Combined with the results presented

DOI: 10.1021/acsami.5b01888
ACS Appl. Mater. Interfaces 2015, 7, 9262−9273

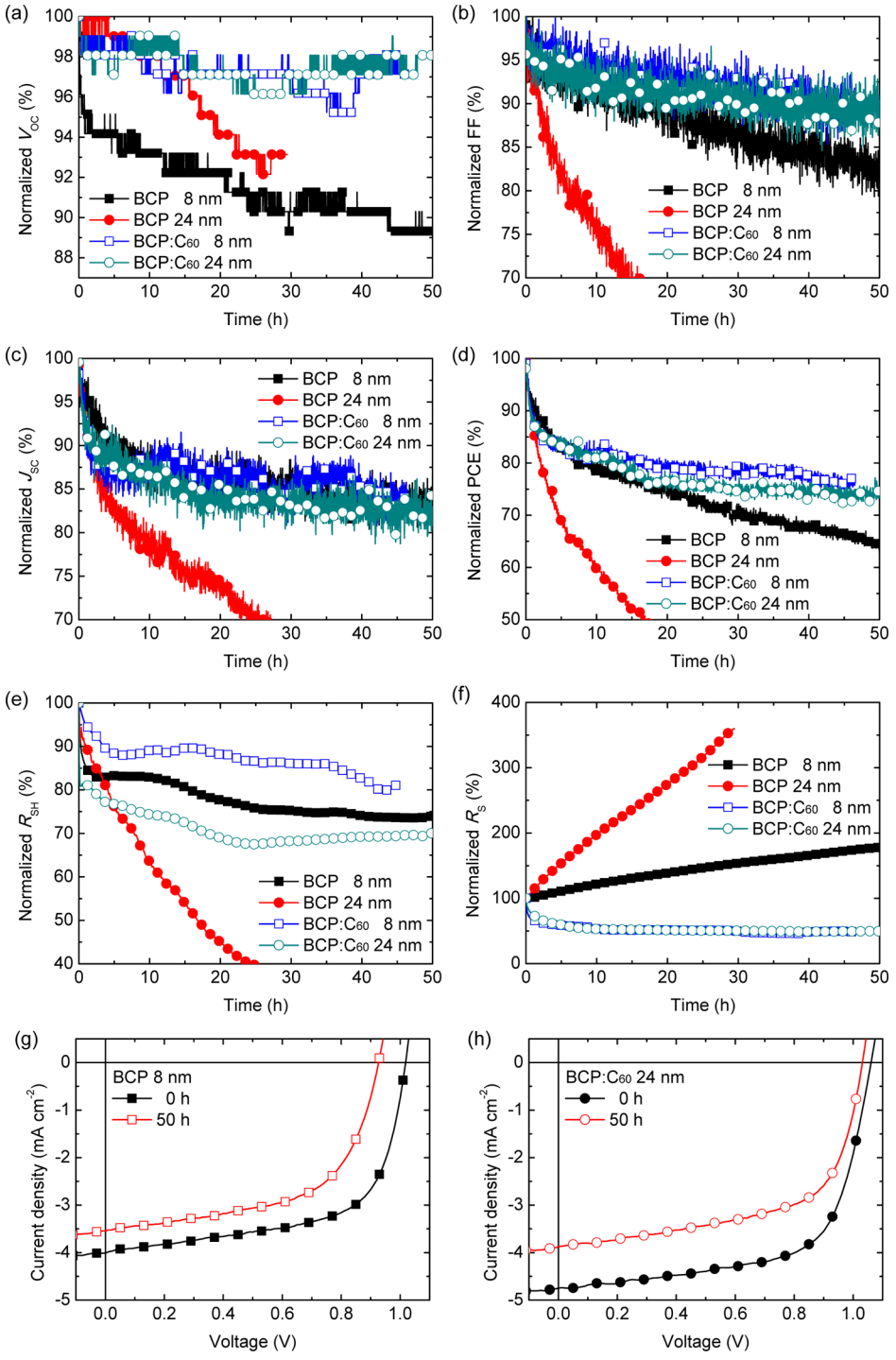

Figure 6. Variation of photovoltaic parameters with time under continuous AM 1.5G solar illumination at 100 mW cm^{-2} for the OPV devices with various buffer layers: (a) V_{OC}, (b) FF, (c) J_{SC}, (d) PCE, (e) R_{SH}, and (f) R_S. All data were normalized to the initial values. Comparison of the OPV device performance before and after continuous AM 1.5G solar illumination at 100 mW cm^{-2} for 50 h: (g) for an 8 nm BCP buffer layer and (h) for a 24 nm BCP:C_{60} buffer layer.

in the preceding paragraph, an optimal buffer layer (in this study, the 24 nm BCP:C_{60}) leads to a reduced interfacial barrier at the C_{60}/buffer layer interface and an increased barrier height at the SubPc/C_{60} interface. In both of these cases, the charge collection efficiency, and hence the device performance, improves considerably. To further quantify the contribution of the improved collection efficiency, charge extraction analysis should be considered.[51] Nevertheless, the observation of the different trend of the improved IQE indicated that excitons in SubPc dissociate more efficiently in devices with a BCP:C_{60} buffer layer than in devices with a neat BCP buffer layer. The analysis of charge extraction may be beyond the scope of the current study.

In addition to the low PCE, the short device lifetime is another factor that has impeded the commercialization of OPV devices. The aforementioned results show that using a 24 nm BCP:C_{60} buffer layer improves the performance, enabling manipulation of the optical properties and increasing the charge

DOI: 10.1021/acsami.5b01888
ACS Appl. Mater. Interfaces 2015, 7, 9262−9273

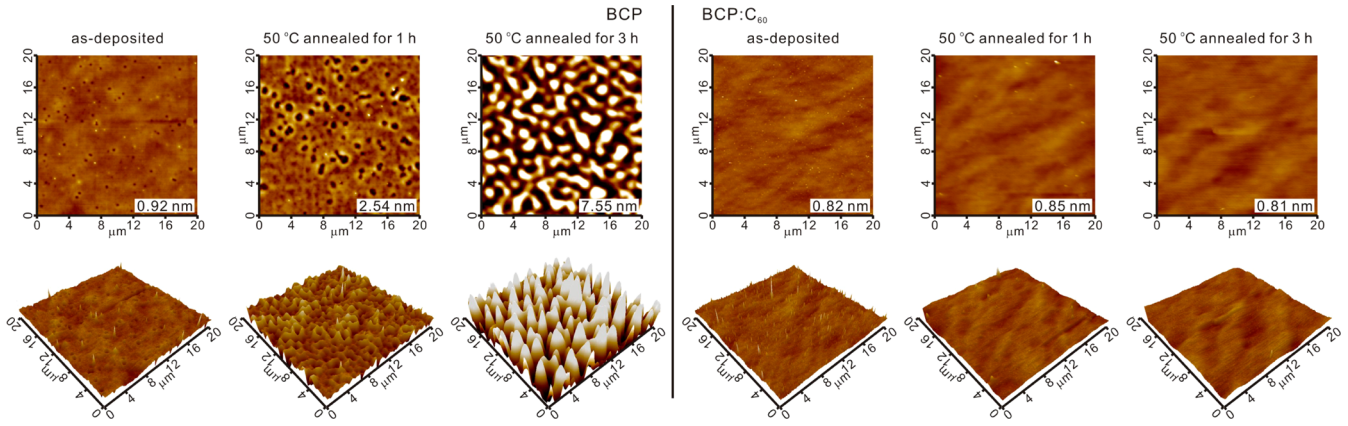

Figure 7. AFM images of 10 nm BCP (left column) and BCP:C_{60} (right column) thin films taken over an area of 20 μm × 20 μm. Both as-deposited and annealed films are shown. The surface roughness of each thin film is indicated in the bottom-right corner. The panels shown at the bottom are the corresponding three-dimensional images.

collection efficiency. In previous studies, inserting anodic buffer layers at the anode/organic interface has increased stability.[52,60−62] Without the anodic buffer layers, oxygen in the ITO may diffuse into the organic layer and penetrate the fullerene, which easily reacts with oxygen.[60] The reduced conductivity caused by the reaction of oxygen and fullerene primarily contributes to a short device lifetime.[63] The formation of defect sites may also occur and enhance carrier recombination, reducing both the PCE and lifetime.[64] In the current study, a thin anodic buffer MoO_3 anodic buffer layer with a thickness of 15 nm was used, this buffer layer reduced the diffusion of oxygen, thereby preventing the device lifetime from decreasing. Previous studies have reported an increase in the device lifetime when the MoO_3 anodic buffer layer is used. However, the device lifetime continuously decreased with the operating time.[52,61,62] A possible reason for the decrease in the lifetime is the use of the BCP buffer layer, which easily crystallizes at an ambient temperature even when the device is stored in a vacuum without being exposed to the atmosphere.[10,65−67] Although mixed buffer layers have been proposed in the literature, the device lifetime has yet to be investigated.[38,39] Here, we compared the variation of the OPV device performance as a function of time for various buffer layers. Figure 6 shows the degradation of the photovoltaic characteristics as a function of time. As shown in Figure 6a,b, the OPV device with a BCP buffer layer showed a monotonic decrease in V_{OC} and the FF, whereas using the BCP:C_{60} buffer layer yielded an almost identical V_{OC} and a small reduction in the FF. The reduction in J_{SC} of these devices was comparable, except for the device with a 24 nm BCP buffer layer, as shown in Figure 6c. However, the OPV device with a BCP:C_{60} buffer layer was stable after an initial rapid decay, unlike the 8 nm BCP device. Therefore, the PCE of the OPV device with a BCP:C_{60} buffer layer showed slow degradation, as shown in Figure 6d. The initial rapid decay observed for both devices could have resulted from several factors such as the fabrication process environment, substrate cleanness, and intrinsic degradation of the materials.[3,68,69] After aging-like degradation, the decay in device performance may be determined by the type of buffer layer used (anodic or cathodic buffer layer). In the current study, MoO_3 was used as an anodic buffer to prevent oxygen diffusion from the ITO electrode. Therefore, the use of a BCP:C_{60} mixed buffer layer may contribute to an increase in the device lifetime. Parts e and f of Figure 6 show the variation of R_{SH} and R_S during the testing time, respectively. The R_{SH} decreased for all devices, and therefore, it is irrelevant with regard to the device performance. However, R_S exhibited an opposite trend for the devices with different types of buffer layers. For the device with a BCP buffer layer, it increased monotonically, whereas for the BCP:C_{60} device, it showed an initial exponential decrease and then stabilized over the testing interval. The increase in R_S was consistent with the continuously decreasing trend observed in the FF, and therefore, it resulted in appreciable degradation of the PCE. The most striking observation is the degradation of the device with a 24 nm BCP buffer layer, which showed a substantial decay for all parameters, thus leading to the poorest device lifetime compared with other devices. This phenomenon will be discussed in detail in the following paragraph. The photo $J-V$ characteristics of the devices with 8 nm BCP and 24 nm BCP:C_{60} buffer layers before and after a 50 h photodegradation process are presented in Figure 6g,h. Although the degradation seems different between the two devices (i.e., the short-circuit current affected more in the mixed buffer than open-circuit voltage), the reduction in percentage for J_{SC} was similar (see Figure 6c). Therefore, the primary degradation of the devices resulted from the change in FF, or R_S.

The parameter R_S is generally related to the contact resistance at the metal/organic layer interface and carrier transportation in organic materials. The discussed devices were fabricated with a SubPc/C_{60} bilayer structure by using various buffer layers. Therefore, the large variation in R_S and the increased lifetime may have resulted from the influence of the BCP:C_{60} buffer layer. Because of its low glass transition temperature, a neat BCP layer is easily crystallized in an ambient environment.[65,67] The crystallization of BCP may delaminate the organic layer and electrode, resulting in poor contact and hence high R_S. Possible evidence of this phenomenon is the observation of a rapid decay for the device with a 24 nm BCP buffer layer. When the thickness of BCP increased from 8 to 24 nm, the crystallization may have been more pronounced, thus leading to the substantial degradation. This inference is consistent with the increasing trend of R_S mentioned in the previous paragraph. By contrast, the device with a BCP:C_{60} buffer layer showed a lower R_S after being illuminated for over 50 h. In addition, an increased lifetime was observed. These results may imply that the blend of BCP and C_{60} suppressed the crystallization of BCP. To confirm this suppression, the morphological changes in the neat BCP and

DOI: 10.1021/acsami.5b01888
ACS Appl. Mater. Interfaces 2015, 7, 9262−9273

BCP:C_{60} mixed layers were investigated using atomic force microscopy (AFM) measurements. An aging process involving thermal annealing at 50 °C was conducted to accelerate the morphological changes in the buffer layers with time. Figure 7 shows AFM images of 10 nm BCP and BCP:C_{60} thin films under various conditions. AFM images of a smaller area (5 μm × 5 μm), where features can be observed in detail are presented in the Supporting Information (Figure S6). Immediately after BCP deposition, the surface showed a pinhole-like feature. The pinhole-like feature can be attributed to an aggregation of BCP molecules[70] and may indicate the ease of crystallization. After the thin film was annealed for 1 h, the pinholes increased in size and were distributed over the entire area. After the thin film annealed for 3 h, the morphology was completely different from that of the as-deposited and 1-h-annealed thin films. The BCP molecules strongly aggregated and formed an island-like morphology. The surface roughness increased from 0.92 and 2.54 to 7.55 nm when the annealing processes were performed. These results suggest that the neat BCP thin film was crystallized and could have degraded the cathodic interface, as indicated by the increasing trend of R_S. By contrast, an as-deposited BCP:C_{60} thin film showed a smoother surface. Except for the as-deposited BCP:C_{60}, which showed few protuberances that are likely to have been formed by C_{60} molecules, the surface morphology was independent of the annealing process. In addition, when the BCP:C_{60} thin film was annealed, the protuberances disappeared. All of the BCP:C_{60} thin films exhibited similar surface roughness of approximately 0.8 nm. The AFM images of the BCP:C_{60} thin film suggests that blending C_{60} into BCP effectively suppressed BCP crystallization, thereby stabilizing the device performance over time and increasing the device lifetime.

CONCLUSION

In summary, we demonstrated the effect of using a BCP:C_{60} cathodic buffer layer on the device performance of small-molecule OPV devices with the bilayer structure SubPc/C_{60}. An optical field simulation suggested that the optical properties can be optimized using a transparent and thick BCP layer. However, when the thickness of the BCP layer was increased, the electrical properties deteriorated considerably, thus impeding optical manipulation. Replacing the conventional BCP with BCP:C_{60} enabled achieving optimal optical properties and improved the PCE from 2.5% to 3.2%. IQE measurements revealed that using the BCP:C_{60} buffer layer enhanced the charge collection efficiency. In addition, increasing the BCP:C_{60} thickness considerably improved the IQE over the entire spectrum. An effective estimation of the interfacial barrier suggested that using C_{60} along with BCP can effectively reduce the injection barrier at the C_{60}/BCP interface, thereby increasing charge collection at the cathode. Temperature-dependent measurement of the OPV devices was performed to calculate the barrier height at the SubPc/C_{60} interface. The results showed that using an optimal buffer layer, 24 nm BCP:C_{60}, increased the barrier height, increasing the possibility of exciton dissociation and J_{SC}. The time-dependent variation of the device performance indicated that using the conventional BCP buffer layer deteriorated the device performance considerably. By contrast, the BCP:C_{60} buffer layer contributed to an increase in the device lifetime. AFM images of both BCP and BCP:C_{60} thin films under various conditions showed a considerable change in the morphology of the neat BCP when it was annealed. By contrast, the morphology of the BCP:C_{60} thin film was almost unchanged because of the suppression of BCP crystallization. Thus, the optimal BCP:C_{60} buffer layer not only improved the device performance but also increased the device lifetime.

EXPERIMENTAL SECTION

Materials and Device Fabrication. All materials—MoO_3, SubPc, C_{60}, BCP, and Al—were purchased from Sigma-Aldrich. The materials were used as received without further purification. ITO glasses that were used as substrates were purchased from Luminescence Technology Corp. The sheet resistance of ITO was approximately 15 Ω/sq. A standard ultrasonic bath in solutions (detergent, deionized water, acetone, and isopropanol) was used to clean the ITO surface. The ITO was subjected to no additional treatment before thin-film deposition. OPV devices were fabricated in a high vacuum chamber with a pressure lower than 8×10^{-6} Torr. A custom-made in situ four-shutter system in which each shutter could be controlled individually enabled fabricating at most four cell parameters in one process to prevent run-to-run deviation. A custom-designed layout enabled the fabrication of five devices on one substrate, preventing substrate-to-substrate and device-to-device variations. The thicknesses and deposition rates of thin films were monitored during the thin-film deposition by using a deposition controller (STM-2XM, Sycon Instruments) with a quartz crystal microbalance. The thickness of each layer was measured using a surface profiler (Veeco Dektak 3) and ellipsometry (Raditech SE-950). The deposition rate of each thin film, except for the BCP:C_{60} layer, was approximately 0.1 nm/s. The BCP:C_{60} thin film was formed with a volume ratio of 1:1, and the deposition rates of both materials were approximately 0.05 nm/s. The active area (0.04 cm^2) of devices was defined through the deposition of Al through a shadow mask. After the fabrication process, the devices were transferred into a nitrogen-filled glovebox. All devices were appropriately encapsulated using a UV-curable epoxy resin (EXC345, Everwide Chemical Co. Ltd.) and a getter-attached glass that fitted the area of epoxy resin. The encapsulation process was completed by exposing the devices to UV illumination.

Device Characterization. All characterizations were performed in an ambient environment. The $J-V$ characteristics in the dark and under AM 1.5G solar illumination provided by a solar simulator (New port 91160A) were measured using a source meter (Keithley 2636A). A monochromator (Newport 74100) and lock-in amplifier (Stanford Research Systems SR830) chopped at 250 Hz were used to measure the EQE spectra. A UV−visible spectrophotometer (Thermo Scientific Evolution 220) equipped with an integrating sphere was used in the reflection mode to measure the total absorption of the OPV devices. The IQE spectra were calculated by dividing the EQE by the absorption. Temperature-dependent measurements were performed in a cooled cryostat (Janis VPF-100) connected to a cryogenic temperature controller (Lake Shore 335).

Thin-Film Characterization. Optical constants, refractive indices, and extinction coefficients were obtained using ellipsometry. The highest occupied molecular orbital (HOMO) levels of organic materials and work functions were estimated using a low energy photoelectron spectrometer (Riken Keiki AC-2). Optical band gaps were estimated using the UV−visible spectrophotometer used for determining the absorption. The LUMO levels were calculated by subtracting the HOMO levels from the optical bad gaps. AFM images were obtained using the Park Systems XE-70 in the noncontact mode. An NCHR type noncontact cantilever with a frequency of 320 kHz, thickness of 4 μm, length of 125 μm, width of 30 μm, and typical tip radius less than 10 nm was used. Thermal annealing processes were performed at 50 °C on a hot plate (M&R Nanotechnology Co. Ltd. AGHP2S).

ASSOCIATED CONTENT

Supporting Information

Optical constants of organic materials, thickness-dependent $J-V$ characteristics of devices using BCP:C_{60} buffer layer, method

DOI: 10.1021/acsami.5b01888
ACS Appl. Mater. Interfaces 2015, 7, 9262−9273

of estimating total absorption, IQE, interfacial barrier, barrier height, and AFM images with a smaller area. This material is available free of charge via the Internet at http://pubs.acs.org.

AUTHOR INFORMATION

Corresponding Authors

*(C.-C.L.) E-mail: cclee@mail.ntust.edu.tw.
*(S.-W.L.) E-mail: swliu@mail.mcut.edu.tw.

Author Contributions

§S.-W.L. and C.-C.L. contributed equally to this work.

Notes

The authors declare no competing financial interest.

ACKNOWLEDGMENTS

We acknowledge financial support from the Ministry of Science and Technology (Grant Nos. MOST 102-2221-E-131-026-MY2, 102-2221-E-131-030-MY2, 102-2221-E-011-142, 102-2511-S-131-002, 102-2622-E-011-018-CC3, 103-ET-E-011-004-ET, 103-2627-E-002-002, 103-2622-E-131-007-CC3, and 104-2623-E-011-001-D). In addition, S.-W.L. is grateful to Mr. H.-H. Wu, Syskey Technology Corp. (Taiwan), for his assistance in designing the fabrication system.

REFERENCES

(1) Kyaw, A. K. K.; Wang, D. H.; Gupta, V.; Leong, W. L.; Ke, L.; Bazan, G. C.; Heeger, A. J. Intensity Dependence of Current−Voltage Characteristics and Recombination in High-Efficiency Solution-Processed Small-Molecule Solar Cells. *ACS Nano* **2013**, *7*, 4569−4577.

(2) Zhou, J.; Zuo, Y.; Wan, X.; Long, G.; Zhang, Q.; Ni, W.; Liu, Y.; Li, Z.; He, G.; Li, C. Solution-Processed and High-Performance Organic Solar Cells Using Small Molecules with a Benzodithiophene Unit. *J. Am. Chem. Soc.* **2013**, *135*, 8484−8487.

(3) Zou, Y.; Holst, J.; Zhang, Y.; Holmes, R. J. 7.9% Efficient Vapor-Deposited Organic Photovoltaic Cells Based on a Simple Bulk Heterojunction. *J. Mater. Chem. A* **2014**, *2*, 12397−12402.

(4) Peumans, P.; Bulović, V.; Forrest, S. Efficient Photon Harvesting at High Optical Intensities in Ultrathin Organic Double-Heterostructure Photovoltaic Diodes. *Appl. Phys. Lett.* **2000**, *76*, 2650−2652.

(5) Rand, B. P.; Li, J.; Xue, J.; Holmes, R. J.; Thompson, M. E.; Forrest, S. R. Organic Double-Heterostructure Photovoltaic Cells Employing Thick Tris (Acetylacetonato) Ruthenium (III) Exciton-Blocking Layers. *Adv. Mater.* **2005**, *17*, 2714−2718.

(6) Chan, M.; Lai, S.; Lau, K.; Lee, C.; Lee, S. Application of Metal-Doped Organic Layer Both as Exciton Blocker and Optical Spacer for Organic Photovoltaic Devices. *Appl. Phys. Lett.* **2006**, *89*, No. 163515.

(7) Chan, M.; Lee, C.; Lai, S.; Fung, M.; Wong, F.; Sun, H.; Lau, K.; Lee, S. Efficient Organic Photovoltaic Devices Using a Combination of Exciton Blocking Layer and Anodic Buffer Layer. *J. Appl. Phys.* **2006**, *100*, No. 094506.

(8) Lassiter, B. E.; Wei, G.; Wang, S.; Zimmerman, J. D.; Diev, V. V.; Thompson, M. E.; Forrest, S. R. Organic Photovoltaics Incorporating Electron Conducting Exciton Blocking Layers. *Appl. Phys. Lett.* **2011**, *98*, No. 243307.

(9) Lin, H.-W.; Kang, H.-W.; Huang, Z.-Y.; Chen, C.-W.; Chen, Y.-H.; Lin, L.-Y.; Lin, F.; Wong, K.-T. An Effective Bilayer Cathode Buffer for Highly Efficient Small Molecule Organic Solar Cells. *Org. Electron.* **2012**, *13*, 1925−1929.

(10) Zhuang, T.; Su, Z.; Liu, Y.; Chu, B.; Li, W.; Wang, J.; Jin, F.; Yan, X.; Zhao, B.; Zhang, F. Improvement of Both Efficiency and Working Lifetime in Organic Photovoltaic Devices by Using Bathophenanthroline/Tin (IV) Phthalocyanine Dichloride as Bilayer Exciton Blocking Layers. *Appl. Phys. Lett.* **2012**, *100*, No. 243902.

(11) Gregg, B. A.; Hanna, M. C. Comparing Organic to Inorganic Photovoltaic Cells: Theory, Experiment, and Simulation. *J. Appl. Phys.* **2003**, *93*, 3605−3614.

(12) Kippelen, B.; Brédas, J.-L. Organic Photovoltaics. *Energy Environ. Sci.* **2009**, *2*, 251−261.

(13) Peumans, P.; Forrest, S. Very-High-Efficiency Double-Heterostructure Copper Phthalocyanine/C_{60} Photovoltaic Cells. *Appl. Phys. Lett.* **2001**, *79*, 126−128.

(14) Pfuetzner, S.; Meiss, J.; Petrich, A.; Riede, M.; Leo, K. Improved Bulk Heterojunction Organic Solar Cells Employing C_{70} Fullerenes. *Appl. Phys. Lett.* **2009**, *94*, No. 223307.

(15) Sakai, J.; Taima, T.; Yamanari, T.; Saito, K. Annealing Effect in the Sexithiophene: C_{70} Small Molecule Bulk Heterojunction Organic Photovoltaic Cells. *Sol. Energy Mater. Sol. Cells* **2009**, *93*, 1149−1153.

(16) Gao, H.; Qin, C.; Zhang, H.; Wu, S.; Su, Z.-M.; Wang, Y. Theoretical Characterization of a Typical Hole/Exciton-Blocking Material Bathocuproine and Its Analogues. *J. Phys. Chem. A* **2008**, *112*, 9097−9103.

(17) Zheng, Y.; Xue, J. Organic Photovoltaic Cells Based on Molecular Donor-Acceptor Heterojunctions. *Polym. Rev.* **2010**, *50*, 420−453.

(18) Sutty, S.; Williams, G.; Aziz, H. Fullerene-Based Schottky-Junction Organic Solar Cells: A Brief Review. *J. Photonics Energy* **2014**, *4*, No. 040999.

(19) Lee, C.-C.; Su, W.-C.; Liu, S.-W.; Yuan, C.-H. Organic Photovoltaic Cells Employing an Ultrathin Electron Donor of Arylamino-Substituted Fumaronitrile Material. *Jpn. J. Appl. Phys.* **2012**, *51*, No. 09MA04.

(20) Lee, C.-C.; Su, W.-C.; Shu, Y.-S.; Chang, W.-C.; Huang, B.-Y.; Lee, Y.-Z.; Su, T.-H.; Chen, K.-T.; Liu, S.-W. Decoupling the Optical and Electrical Properties of Subphthalocyanine/C_{70} Bi-Layer Organic Photovoltaic Devices: Improved Photocurrent While Maintaining a High Open-Circuit Voltage and Fill Factor. *RSC Adv.* **2015**, *5*, 5617−5626.

(21) O'Connor, B.; An, K. H.; Pipe, K. P.; Zhao, Y.; Shtein, M. Enhanced Optical Field Intensity Distribution in Organic Photovoltaic Devices Using External Coatings. *Appl. Phys. Lett.* **2006**, *89*, No. 233502.

(22) Monestier, F.; Simon, J.-J.; Torchio, P.; Escoubas, L.; Ratier, B.; Hojeij, W.; Lucas, B.; Moliton, A.; Cathelinaud, M.; Defranoux, C.; Flory, F. Optical Modeling of Organic Solar Cells Based on Cupc and C_{60}. *Appl. Opt.* **2008**, *47*, C251−C256.

(23) Chen, D.; Zhang, C.; Wang, Z.; Zhang, J.; Feng, Q.; Xu, S.; Zhou, X.; Hao, Y. Performance Comparison of Conventional and Inverted Organic Bulk Heterojunction Solar Cells from Optical and Electrical Aspects. *IEEE Trans. Electron Devices* **2013**, *60*, 451−457.

(24) Wöbkenberg, P. H.; Bradley, D. D.; Kronholm, D.; Hummelen, J. C.; de Leeuw, D. M.; Cölle, M.; Anthopoulos, T. D. High Mobility N-Channel Organic Field-Effect Transistors Based on Soluble C_{60} and C_{70} Fullerene Derivatives. *Synth. Met.* **2008**, *158*, 468−472.

(25) Xi, X.; Li, W.; Wu, J.; Ji, J.; Shi, Z.; Li, G. A Comparative Study on the Performances of Small Molecule Organic Solar Cells Based on Cupc/C_{60} and Cupc/C_{70}. *Sol. Energy Mater. Sol. Cells* **2010**, *94*, 2435−2441.

(26) Vogel, M.; Doka, S.; Breyer, C.; Lux-Steiner, M. C.; Fostiropoulos, K. On the Function of a Bathocuproine Buffer Layer in Organic Photovoltaic Cells. *Appl. Phys. Lett.* **2006**, *89*, No. 163501.

(27) Gommans, H.; Verreet, B.; Rand, B. P.; Muller, R.; Poortmans, J.; Heremans, P.; Genoe, J. On the Role of Bathocuproine in Organic Photovoltaic Cells. *Adv. Funct. Mater.* **2008**, *18*, 3686−3691.

(28) Huang, J.; Yu, J.; Lin, H.; Jiang, Y. Detailed Analysis of Bathocuproine Layer for Organic Solar Cells Based on Copper Phthalocyanine and C_{60}. *J. Appl. Phys.* **2009**, *105*, No. 073105.

(29) Liu, S.-W.; Su, W.-C.; Lee, C.-C.; Cheng, C.-W.; Chou, C.-C.; Lin, C.-F. Origin of the Improved Power Conversion Efficiency of Pentacene/C_{60} Heterojunction Photovoltaic Devices through the Purification of Donor Material. *Jpn. J. Appl. Phys.* **2013**, *52*, No. 041602.

(30) Wang, N.; Yu, J.; Zang, Y.; Huang, J.; Jiang, Y. Effect of Buffer Layers on the Performance of Organic Photovoltaic Cells Based on Copper Phthalocyanine and C_{60}. *Sol. Energy Mater. Sol. Cells* **2010**, *94*, 263−266.

DOI: 10.1021/acsami.5b01888
ACS Appl. Mater. Interfaces 2015, 7, 9262−9273

(31) Liu, Y.; Ren, Q.; Su, Z.; Chu, B.; Li, W.; Wu, S.; Jin, F.; Zhao, B.; Yan, X.; Wang, J. The Working Mechanism of Organic Photovoltaic Cell by Using Copper Phthalocyanine as Exciton Blocking Layer. *Org. Electron.* **2012**, *13*, 2156−2159.
(32) Mityashin, A.; Cheyns, D.; Rand, B. P.; Heremans, P. Understanding Metal Doping for Organic Electron Transport Layers. *Appl. Phys. Lett.* **2012**, *100*, No. 053305.
(33) Verreet, B.; Malinowski, P. E.; Niesen, B.; Cheyns, D.; Heremans, P.; Stesmans, A.; Rand, B. P. Improved Cathode Buffer Layer to Decrease Exciton Recombination in Organic Planar Heterojunction Solar Cells. *Appl. Phys. Lett.* **2013**, *102*, No. 043301.
(34) Forrest, S. R. The Limits to Organic Photovoltaic Cell Efficiency. *MRS Bull.* **2005**, *30*, 28−32.
(35) Yoo, S.; Potscavage, W. J.; Domercq, B.; Han, S.-H.; Jones, S. C.; Szoszkiewicz, R.; Levi, D.; Riedo, E.; Marder, S. R.; Kippelen, B. Analysis of Improved Photovoltaic Properties of Pentacene/C_{60} Organic Solar Cells: Effects of Exciton Blocking Layer Thickness and Thermal Annealing. *Solid-State Electron.* **2007**, *51*, 1367−1375.
(36) Luo, D.; Yu, L.; Man, J.; Liu, T.; Li, J.; Xu, T.; Liu, Z.; Wang, Z.; Lu, Z. A Bi-Functional Structure with Tunable Electrical and Optical Properties for Organic Photovoltaic Cells. *J. Appl. Phys.* **2013**, *113*, No. 224506.
(37) Menke, S. M.; Lindsay, C. D.; Holmes, R. J. Optical Spacing Effect in Organic Photovoltaic Cells Incorporating a Dilute Acceptor Layer. *Appl. Phys. Lett.* **2014**, *104*, No. 243302.
(38) Bartynski, A. N.; Trinh, C.; Panda, A.; Bergemann, K.; Lassiter, B. E.; Zimmerman, J. D.; Forrest, S. R.; Thompson, M. E. A Fullerene-Based Organic Exciton Blocking Layer with High Electron Conductivity. *Nano Lett.* **2013**, *13*, 3315−3320.
(39) Xiao, X.; Bergemann, K. J.; Zimmerman, J. D.; Lee, K.; Forrest, S. R. Small-Molecule Planar-Mixed Heterojunction Photovoltaic Cells with Fullerene-Based Electron Filtering Buffers. *Adv. Energy Mater.* **2014**, *4*, No. 1301557.
(40) Pettersson, L. A.; Roman, L. S.; Inganas, O. Modeling Photocurrent Action Spectra of Photovoltaic Devices Based on Organic Thin Films. *J. Appl. Phys.* **1999**, *86*, 487−496.
(41) Mutolo, K. L.; Mayo, E. I.; Rand, B. P.; Forrest, S. R.; Thompson, M. E. Enhanced Open-Circuit Voltage in Subphthalocyanine/C_{60} Organic Photovoltaic Cells. *J. Am. Chem. Soc.* **2006**, *128*, 8108−8109.
(42) Perez, M. D.; Borek, C.; Forrest, S. R.; Thompson, M. E. Molecular and Morphological Influences on the Open Circuit Voltages of Organic Photovoltaic Devices. *J. Am. Chem. Soc.* **2009**, *131*, 9281−9286.
(43) Nelson, J.; Kirkpatrick, J.; Ravirajan, P. Factors Limiting the Efficiency of Molecular Photovoltaic Devices. *Phys. Rev. B* **2004**, *69*, No. 035337.
(44) Ravirajan, P.; Haque, S.; Durrant, J.; Poplavskyy, D.; Bradley, D.; Nelson, J. Hybrid Nanocrystalline Tio_2 Solar Cells with a Fluorene−Thiophene Copolymer as a Sensitizer and Hole Conductor. *J. Appl. Phys.* **2004**, *95*, 1473−1480.
(45) Jin, H.; Tuomikoski, M.; Hiltunen, J.; Kopola, P.; Maaninen, A.; Pino, F. Polymer−Electrode Interfacial Effect on Photovoltaic Performances in Poly(3-hexylthiophene): Phenyl-C61-Butyric Acid Methyl Ester Based Solar Cells. *J. Phys. Chem. C* **2009**, *113*, 16807−16810.
(46) Kumar, A.; Sista, S.; Yang, Y. Dipole Induced Anomalous S-Shape *I*−*V* Curves in Polymer Solar Cells. *J. Appl. Phys.* **2009**, *105*, No. 094512.
(47) Tress, W.; Petrich, A.; Hummert, M.; Hein, M.; Leo, K.; Riede, M. Imbalanced Mobilities Causing S-Shaped IV Curves in Planar Heterojunction Organic Solar Cells. *Appl. Phys. Lett.* **2011**, *98*, No. 063301.
(48) Wang, J.; Ren, X.; Shi, S.; Leung, C.; Chan, P. K. Charge Accumulation Induced S-Shape J−V Curves in Bilayer Heterojunction Organic Solar Cells. *Org. Electron.* **2011**, *12*, 880−885.
(49) Lin, C.-F.; Liu, S.-W.; Lee, C.-C.; Hunag, J.-C.; Su, W.-C.; Chiu, T.-L.; Chen, C.-T.; Lee, J.-H. Open-Circuit Voltage and Efficiency Improvement of Subphthalocyanine-Based Organic Photovoltaic Device through Deposition Rate Control. *Sol. Energy Mater. Sol. Cells* **2012**, *103*, 69−75.
(50) Liu, S.-W.; Su, W.-C.; Lee, C.-C.; Chou, C.-C.; Cheng, C.-W. Efficient Organic Photovoltaic Device Using a Sublimated Subphthalocyanine as an Electron Donor. *ECS Solid State Lett.* **2012**, *1*, P70−P72.
(51) Credgington, D.; Liu, S.-W.; Nelson, J.; Durrant, J. R. In Situ Measurement of Energy Level Shifts and Recombination Rates in Subphthalocyanine/C_{60} Bilayer Solar Cells. *J. Phys. Chem. C* **2014**, *118*, 22858−22864.
(52) Su, W.-C.; Lee, C.-C.; Liu, S.-W.; Lin, C.-F.; Chou, C.-C.; Huang, B.-Y.; Cheng, C.-W. Improving the Performance of Subphthalocyanine/C_{60} Planar Heterojunction Organic Photovoltaic Device through the Insertion of Molybdenum Oxide Anodic Buffer. *Jpn. J. Appl. Phys.* **2014**, *53*, No. 03CE02.
(53) Burkhard, G. F.; Hoke, E. T.; McGehee, M. D. Accounting for Interference, Scattering, and Electrode Absorption to Make Accurate Internal Quantum Efficiency Measurements in Organic and Other Thin Solar Cells. *Adv. Mater.* **2010**, *22*, 3293−3297.
(54) Wagner, J.; Gruber, M.; Hinderhofer, A.; Wilke, A.; Bröker, B.; Frisch, J.; Amsalem, P.; Vollmer, A.; Opitz, A.; Koch, N. High Fill Factor and Open Circuit Voltage in Organic Photovoltaic Cells with Diindenoperylene as Donor Material. *Adv. Funct. Mater.* **2010**, *20*, 4295−4303.
(55) Pandey, R.; Gunawan, A. A.; Mkhoyan, K. A.; Holmes, R. J. Efficient Organic Photovoltaic Cells Based on Nanocrystalline Mixtures of Boron Subphthalocyanine Chloride and C60. *Adv. Funct. Mater.* **2012**, *22*, 617−624.
(56) Hong, I.-H.; Lee, M.-W.; Koo, Y.-M.; Jeong, H.; Kim, T.-S.; Song, O.-K. Effective Hole Injection of Organic Light-Emitting Diodes by Introducing Buckminsterfullerene on the Indium Tin Oxide Anode. *Appl. Phys. Lett.* **2005**, *87*, No. 063502.
(57) Yoo, S.; Domercq, B.; Kippelen, B. Intensity-Dependent Equivalent Circuit Parameters of Organic Solar Cells Based on Pentacene and C_{60}. *J. Appl. Phys.* **2005**, *97*, No. 103706.
(58) Potscavage, W. J., Jr; Yoo, S.; Kippelen, B. Origin of the Open-Circuit Voltage in Multilayer Heterojunction Organic Solar Cells. *Appl. Phys. Lett.* **2008**, *93*, No. 193308.
(59) Giebink, N. C.; Wiederrecht, G. P.; Wasielewski, M. R.; Forrest, S. R. Ideal Diode Equation for Organic Heterojunctions. I. Derivation and Application. *Phys. Rev. B* **2010**, *82*, No. 155305.
(60) Lo, M. F.; Ng, T. W.; Lai, S.; Fung, M. K.; Lee, S. T.; Lee, C. S. Stability Enhancement in Organic Photovoltaic Device by Using Polymerized Fluorocarbon Anode Buffer Layer. *Appl. Phys. Lett.* **2011**, *99*, No. 033302.
(61) Dong, W. J.; Jung, G. H.; Lee, J.-L. Solution-Processed-Moo_3 Hole Extraction Layer on Oxygen Plasma-Treated Indium Tin Oxide in Organic Photovoltaics. *Sol. Energy Mater. Sol. Cells* **2013**, *116*, 94−101.
(62) Huang, P.-H.; Huang, C.-J.; Chen, K.-L.; Ke, J.-C.; Wang, Y.-H.; Kang, C.-C. Improved Reliability of Small Molecule Organic Solar Cells by Double Anode Buffer Layers. *J. Nanomaterials* **2014**, *2014*, No. 741761.
(63) Ng, T.; Lo, M.; Zhou, Y.; Liu, Z.; Lee, C.; Kwon, O.; Lee, S. Ambient Effects on Fullerene/Copper Phthalocyanine Photovoltaic Interface. *Appl. Phys. Lett.* **2009**, *94*, No. 193304.
(64) Hamed, A.; Sun, Y.; Tao, Y.; Meng, R.; Hor, P. Effects of Oxygen and Illumination on the in Situ Conductivity of C_{60} Thin Films. *Phys. Rev. B* **1993**, *47*, 10873−10880.
(65) Lee, C.-C.; Su, W.-C.; Huang, J.-C.; Lin, C.-F.; Liu, S.-W. Degradation Mechanism of Organic Photovoltaic Devices with Bathocuproine Buffer Layer. *J. Photonics Energy* **2011**, *1*, No. 011108.
(66) Jin, F.; Chu, B.; Li, W.; Su, Z.; Zhao, B.; Yan, X.; Zhang, F.; Fan, D.; Zhang, T.; Gao, Y. Improvement in Power Conversion Efficiency and Long-Term Lifetime of Organic Photovoltaic Cells by Using Bathophenanthroline/Molybdenum Oxide as Compound Cathode Buffer Layer. *Sol. Energy Mater. Sol. Cells* **2013**, *117*, 189−193.
(67) Liu, S.-W.; Lee, C.-C.; Lin, C.-F.; Huang, J.-C.; Chen, C.-T.; Lee, J.-H. 4-Hydroxy-8-Methyl-1,5-Naphthyridine Aluminium Chelate:

DOI: 10.1021/acsami.5b01888
ACS Appl. Mater. Interfaces 2015, 7, 9262−9273

A Morphologically Stable and Efficient Exciton-Blocking Material for Organic Photovoltaics with Prolonged Lifetime. *J. Mater. Chem.* **2010**, *20*, 7800−7806.
(68) Ebadian, S.; Gholamkhass, B.; Shambayati, S.; Holdcroft, S.; Servati, P. Effects of Annealing and Degradation on Regioregular Polythiophene-Based Bulk Heterojunction Organic Photovoltaic Devices. *Sol. Energy Mater. Sol. Cells* **2010**, *94*, 2258−2264.
(69) AL-Amar, M. M.; Hamam, K. J.; Mezei, G.; Guda, R.; Hamdan, N. M.; Burns, C. A. A New Method to Improve the Lifetime Stability of Small Molecule Bilayer Heterojunction Organic Solar Cells. *Sol. Energy Mater. Sol. Cells* **2013**, *109*, 270−274.
(70) Liu, S.-W.; Su, W.-C.; Lee, C.-C.; Lin, C.-F.; Cheng, C.-W.; Chou, C.-C.; Lee, J.-H.; Chen, C.-T. Enhancement in Open Circuit Voltage of Organic Photovoltaic Devices through Control of Deposition Rate of Donor Material. *Sol. Energy Mater. Sol. Cells* **2013**, *109*, 280−287.

DOI: 10.1021/acsami.5b01888
ACS Appl. Mater. Interfaces 2015, 7, 9262−9273